Supplementary Material to Paper: "Imaging with Confidence: Uncertainty Quantification for High-dimensional Undersampled MR Images"

Frederik Hoppe[1*], Claudio Mayrink Verdun[2*], Hannah Laus[3*], Sebastian Endt[4], Marion I. Menzel[4], Felix Krahmer[3], and Holger Rauhut[5]

[1] RWTH Aachen University, Germany hoppe@mathc.rwth-aachen.de
[2] Harvard University, USA claudioverdun@seas.harvard.edu
[3] TU Munich & MCML, Germany {hannah.laus,felix.krahmer}@tum.de
[4] TH Ingolstadt, TU Munich & GE HealthCare, Germany {sebastian.endt,Marion.Menzel}@thi.de
[5] LMU Munich & MCML, Germany rauhut@math.lmu.de

The supplementary material is structured as follows: In Section 1, we explain the connection between the one-dimensional theory used for describing our method in the main paper and the two-dimensional practical implementation with which we conduct our experiments. Section 2 provides a detailed construction for the three confidence sets introduced in Section 5 of the main paper. Finally, in Section 3, we analyze the results of the experiments mentioned in Section 7 of the main paper and add more experiments supporting our results.

1 Bridging 1D Theory with 2D Practical Implementation

For clarity, the description of our method *Imaging with Confidence* is written for images reshaped as vectors $x^0 \in \mathbb{C}^N$. However, in our experiments, we consider the 2D structure of the images, here represented without loss of generality, as $\sqrt{N} \times \sqrt{N}$-matrices. In this paper, $\mathcal{F}$ denotes the 1D DFT matrix applied to vectors $x^0 \in \mathbb{C}^N$.

Therefore, for an image $X^0 \in \mathbb{C}^{\sqrt{N}\times\sqrt{N}}$ the 2D FFT $\mathcal{F}$ is given by $B = \mathcal{F}(X^0) = FX^0F^T$, where $F \in \mathbb{C}^{\sqrt{N}\times\sqrt{N}}$ is the discrete Fourier matrix. This means that a two-dimensional Fourier transform takes the Fourier transform of the column vectors, and afterward, the FFT is applied to the rows. In vectorized shape $b = \text{vector}(B) = (F \otimes F)x^0$, where $\otimes$ denotes the Kronecker product. See [3, Chapter 5] for more details. Then, the subsampling step with a mask $\mathcal{P} \in \mathbb{C}^{\sqrt{N}\times\sqrt{N}}$ is equivalent to selecting the corresponding rows of $F \otimes F$.

The total variation minimization problem exploits sparsity in the finite gradient domain. In 2D, we define the finite gradient for both directions as

$$D_x = (X^0_{i2} - X^0_{i1}, X^0_{i3} - X^0_{i2}, \cdots, X^0_{i\sqrt{N}} - X^0_{i\sqrt{N}-1}), \quad i \in \{1, \ldots, \sqrt{N}\} \tag{1}$$

and

$$D_y = (X^0_{2j} - X^0_{1j}, X^0_{3j} - X^0_{2j}, \cdots, X^0_{\sqrt{N}j} - X^0_{\sqrt{N}-1j}), \quad j \in \{1, \ldots, \sqrt{N}\}. \tag{2}$$

[*] These authors contributed equally to this work.

Algorithm 1 Split-Bregman for total variation minimization [9]

Input: Sampling mask $\mathcal{P}$, k-space data b, regularization parameter μ, λ_1, λ_2, number of inner and outer iterations n_i, n_o
Initialize $\beta_1^0 = \beta_2^0 = 0$ and $x^0 = y_1^0 = y_2^0 = 0$
for $k = 1, \dots, n_o - 1$ **do**
    solve $(x^{k+1}, y_1^{k+1}, y_2^{k+1}) \leftarrow \arg\min_{x,y_1,y_2} \|b - \mathcal{P}\mathcal{F}x\|_2^2 + \frac{\sqrt{\lambda_1}}{\sqrt{\mu}}\|y_1 - D_x x - \beta_1^k\|_2^2 + \frac{\sqrt{\lambda_1}}{\sqrt{\mu}}\|y_2 - D_y x - \beta_2^k\|_2^2 + \|y_1\|_1 + \|y_2\|_1$ using the LSQR algorithm [8] and a shrinkage algorithm n_i times
    $\beta_1^{k+1} = \beta_1^k + (D_x x^{k+1} - y^{k+1})$
    $\beta_2^{k+1} = \beta_2^k + (D_y x^{k+1} - y^{k+1})$
    if $\|x^k - x^{k+1}\|_2 < tol$ **then return** x^{k+1}
    end if
end for
Output: Reconstruction x^{n_o}

Consequently, the two dimensional TV-norm is defined as

$$\|X^0\|_{TV} = \|D_x X^0\|_1 + \|D_y X^0\|_1.$$

We retrieve the images by solving the optimization problem

$$\min_{X \in \mathbb{C}^{\sqrt{N} \times \sqrt{N}}} \frac{\mu}{2}\|\hat{B} - \mathcal{P}\mathcal{F}X\|_2^2 + \lambda_1 \|D_x X\|_1 + \lambda_2 \|D_y X\|_1.$$

with $\hat{B} = \mathcal{P}B$ and $\lambda_1, \lambda_2, \mu > 0$. We minimize such a function with the Split-Bregman algorithm [6], which is also tailored to solve problems with complex data and complex measurement matrices, as is the case in MRI.

For our experiments we set $\lambda_1 = \lambda_2 = 0.05$ and $\mu = \frac{\sqrt{m}}{20\sigma\sqrt{12 \log N}}$. Since the Split-Bregman algorithm (see Algorithm 1) can handle an additional convex function in the ℓ_1-norm, it is a standard method for solving the total variation problem, in particular total variation denoising [4].

2 Construction of Confidence Intervals for Magnitude and Phase

In this section, we provide a more detailed construction of the confidence region and show how to project the two-dimensional confidence region onto one-dimensional confidence intervals for the magnitude and the phase. Let x_i^0 be the true parameter, with $|x_i^0|$ denoting its magnitude and φ_i^0 its phase. Furthermore, let $\hat{x}_i^u$ be the debiased reconstruction with $|\hat{x}_i^u|$ as its magnitude and $\hat{\varphi}_i$ as its phase. First, we construct the confidence regions $C_i(\alpha)$ for the complex pixel x_i^0 by exploiting the Gaussianity of the debiased estimator, *i.e.*

$$\hat{x}^u - x^0 \sim \mathcal{CN}\left(0, \frac{\sigma^2}{m} M \hat{\Sigma} M^*\right), \qquad \hat{\Sigma} := \frac{(\mathcal{P}\mathcal{F})^*(\mathcal{P}\mathcal{F})}{m}. \tag{3}$$

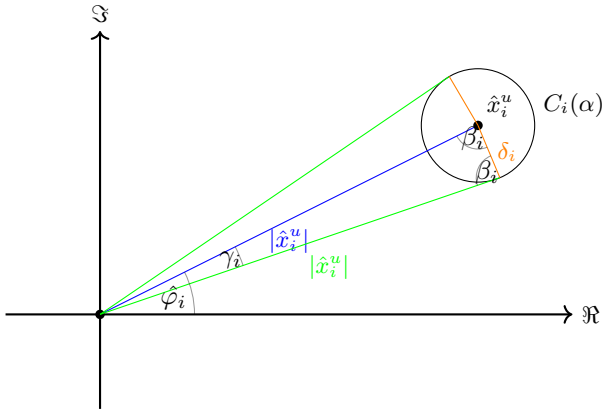

Fig. 1: Sketch of confidence region and related angles.

By definition, $\Re(\hat{x}^u - x^0), \Im(\hat{x}^u - x^0) \sim \mathcal{N}(0, \frac{\sigma^2}{2m} M\hat{\Sigma}M^*)$. Hence, by [1] the difference

$$|\hat{x}_i^u - x_i^0| = \sqrt{\Re(\hat{x}_i^u - x_i^0)^2 + \Im(\hat{x}_i^u - x_i^0)^2} \tag{4}$$

follows a Rayleigh distribution with variance $\frac{\sigma\sqrt{(M\hat{\Sigma}M^*)_{ii}}}{\sqrt{2m}}$, i.e., zero mean Rice distribution with the same variance.

Then, denoting by $C_i(\alpha) := \{z \in \mathbb{C} \mid |\hat{x}_i^u - z| \leq \delta_i(\alpha)\}$, we obtain

$$\mathbb{P}(x_i^0 \in C_i(\alpha)) = \mathbb{P}(|\hat{x}_i^u - x_i^0| \leq \delta_i(\alpha)) \tag{5}$$

$$= \frac{2}{\sigma^2 m (M\hat{\Sigma}M^*)_{ii}} \int_{\delta_i(\alpha)}^{\infty} x \exp\left(-\frac{x^2}{\sigma^2 m (M\hat{\Sigma}M^*)_{ii}}\right) dx \tag{6}$$

$$= \int_{\frac{\delta_i(\alpha)^2}{\sigma^2 m (M\hat{\Sigma}M^*)_{ii}}}^{\infty} \exp(-u) du = \exp\left(-\frac{\delta_i(\alpha)^2}{\sigma^2 m (M\hat{\Sigma}M^*)_{ii}}\right). \tag{7}$$

Therefore, a confidence interval with significance level α will be produced when $\exp\left(-\frac{\delta_i(\alpha)^2}{\sigma^2 m (M\hat{\Sigma}M^*)_{ii}}\right) = \alpha$. This is, in turn, equivalent to

$$\delta_i(\alpha) = \frac{\sigma\sqrt{(M\hat{\Sigma}M^*)_{ii}}}{\sqrt{m}} \sqrt{\log\left(\frac{1}{\alpha}\right)}. \tag{8}$$

To derive the confidence intervals for the magnitude, we note that if $x_i^0 \in C_i(\alpha)$, then the reverse triangle inequality yields

$$\big||x_i^0| - |\hat{x}_i^u|\big| \leq |x_i^0 - \hat{x}_i^u| < \delta, \tag{9}$$

which implies

$$|x_i^0| \in [|\hat{x}_i^u| - \delta_i, |\hat{x}_i^u| + \delta_i]\,. \tag{10}$$

Therefore,

$$\mathbb{P}\left(|x_i^0| \in [|\hat{x}_i^u| - \delta_i(\alpha), |\hat{x}_i^u| + \delta_i(\alpha)]\right) \geq \mathbb{P}(x_i^0 \in C_i(\alpha)) \geq 1 - \alpha. \tag{11}$$

Given a certain entry $|\hat{x}_i^u| > 0$ and a certain confidence region $C_i(\alpha)$, illustrated in Fig. 1, the derivation of the confidence interval for the phase $\varphi_i^0 \in [0, 2\pi)$ can be done as follows. We first note that the following implication holds

$$x_i^0 \in C_i(\alpha) \implies \varphi_i^0 \in [\hat{\varphi}_i - \gamma_i, \hat{\varphi}_i + \gamma_i]. \tag{12}$$

Hence, it remains to determine $\hat{\varphi}_i$ and γ_i. The estimate $\hat{\varphi}_i$ is determined by the real part of $\hat{x}_i^u$ and its magnitude

$$\hat{\varphi}_i = \arcsin\left(\frac{\Re(\hat{x}_i^u)}{|\hat{x}_i^u|}.\right) \tag{13}$$

To calculate γ_i, we apply the law of cosines which yields

$$\delta_i^2 = 2|\hat{x}_i^u|^2 - 2|\hat{x}_i^u|^2\cos(\gamma_i) = 2|\hat{x}_i^u|^2(1 - \cos(\gamma_i)). \tag{14}$$

Then, algebraic manipulation leads to

$$\gamma_i = \arccos\left(1 - \frac{\delta_i^2}{2|\hat{x}_i^u|^2}\right). \tag{15}$$

3 Detailed Results of the Experiments

In this section, we discuss our numerical experiments in further detail. Our algorithm was implemented in Python using PyLops [9]. In particular, we implemented Split-Bregman [6] and FISTA [2] algorithms for the image reconstruction and the nodewise LASSO for constructing a correction matrix M. We run the experiments on a desktop with AMD EPYC 7F52 16-Core CPUs and NVIDIA A100 PCIe030 030 40GB GPUs. We used the code by Genzel et al. [5] to create the radial mask. Our code is available on GitHub (`https://github.com/HannahLaus/Project_UQ_TV.git`).

As mentioned in Section 7 of the main paper, we conducted the described experiments several times, each time with a different realization of the noise vector ε. For the spiral case, we choose subsampling rates of 43% and 62%. In the radial undersampling setting, the masks select 50%, 70%, and 90% of the k-space data. For each sampling mask, the experiments are run with $\sigma = 0.15$ and $\sigma = 0.1$. The resulting relative noise levels $\frac{\|\varepsilon\|_2}{\|P\mathcal{F}x^0\|_2}$ are stated in Tab. 1 for spiral and in Tab. 2 for radial sampling, respectively. In every experiment, we compute the ℓ_2 and ℓ_∞-norm of

- the errors $\hat{x} - x^0$ and $\hat{x}^u - x^0$,

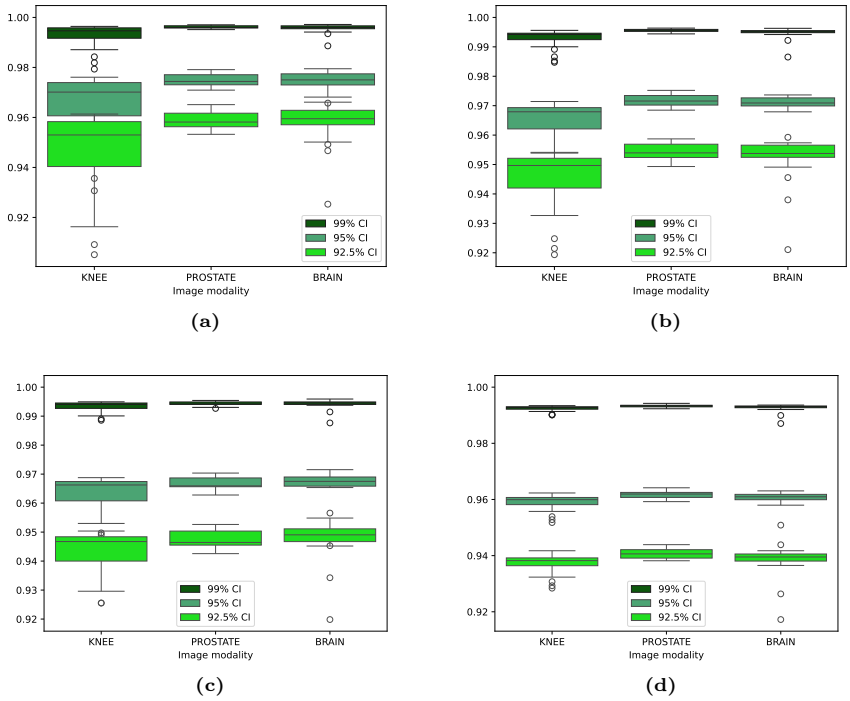

Fig. 2: Box plots for hit rates of CI of different body parts of 25 slices from 5 different patients. Data was reconstructed with either spiral or radial mask with different acceleration factors and 11% noise. 2a Boxplot for reconstruction with spiral mask with 33% undersampling 2b Boxplot for reconstruction with radial mask with 50% undersampling 2c Boxplot for reconstruction with spiral mask with 50% undersampling 2d Boxplot for reconstruction with radial mask with 70% undersampling.

- the remainder term $R := (M\hat{\Sigma} - I_{N\times N})(\hat{x} - x^0)$,
- the Gaussian term $W := \frac{1}{m} M(P\mathcal{F})^* \varepsilon$.

After running 100 iterations, the quantities are averaged. First, we analyze these averaged results for radial sampling in Tab. 2. Not surprisingly, the SSIM increases with the amount of available data, *i.e.*, the amount of k-space points. The less this data is affected by noise, the better the reconstruction and, hence, the larger the SSIM. Another important property is the quality of the debiased estimator in comparison with the biased estimator. One observes that the ℓ_2-error of the debiased estimator is significantly larger. However, the error of the estimator, when measured in the ℓ_∞-norm, is smaller compared to the one given the biased estimator. This is precisely what is required for constructing precise pixel-wise confidence intervals since it determines how far from a random variable, which is Gaussian distribution, the difference $\hat{x}^u - x^0$ is. Moreover, the

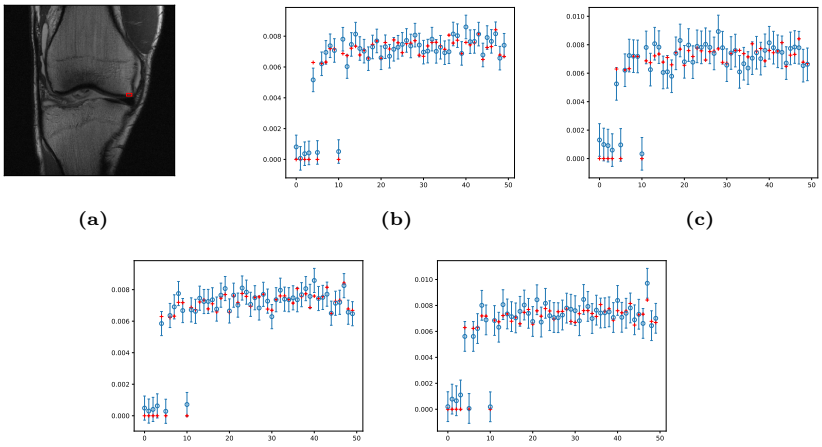

Fig. 3: Confidence intervals for knee image from the fastMRI single-coil dataset [7, 12] for spiral and radial masks and different noise realizations. 95% confidence intervals for the magnitude of pixels in the rectangle. The red crosses are the ground truth values, and the blue circles are the corresponding estimates of the debiased TV estimator. 3a Ground truth image with a rectangle for showing confidence intervals for pixels in the rectangle 3b Reconstruction with 7% noise and 50% radial subsampling 3c Reconstruction with 11% noise and 50% radial subsampling 3d Reconstruction with 7% noise and 50% spiral subsampling 3e Reconstruction with 11% noise and 50% spiral subsampling.

error R is always smaller than the original error $\hat{x} - x^0$, and it decreases when more measurements m are available or the noise gets smaller.

The ratio $\frac{\|R\|_\infty}{\|W\|_\infty}$ impacts the hit rates. In particular, this ratio is smaller in a noisy setting. On the ground truth support, the hit rates for $\sigma = 0.1$ are slightly below those for $\sigma = 0.15$. The lowest hit rate for the support is almost 92%, and it is observed when only 50% k-space samples are available, and the noise level is 7%. Similar results can be observed for spiral sampling in Tab. 1.

To robustify our claims, we conducted further experiments with other image modalities. In particular, we use images from the knee, brain, and prostate NYU fastMRI database [6]. The original database contained a brain and a knee dataset and was created to test the applicability of machine learning on medical image reconstruction; more information about those two datasets can be found in the following two papers [7, 12]. Recently, a third dataset was added

[6] The data used for the experiments in this section were obtained from the NYU fastMRI Initiative database (fastmri.med.nyu.edu) [7,11,12]. The data was provided by the NYU fastMRI investigators but they did not take part in writing or any other contribution of this paper. Under fastmri.med.nyu.edu, the NYU fastMRI investigators are listed; the list is subject to updates.

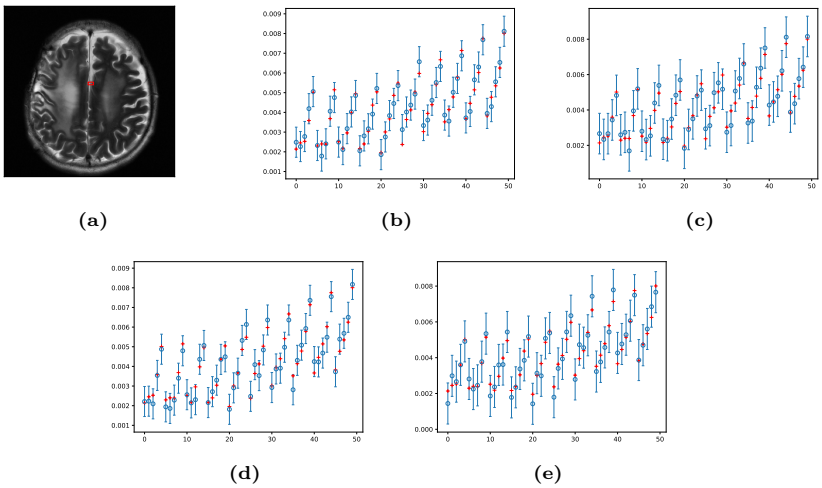

Fig. 4: Confidence intervals for brain image from the fastMRI multi-coil dataset [7,12] for spiral and radial masks and different noise realizations. 95% confidence intervals for the magnitude of pixels in the rectangle. The red crosses are the ground truth values, and the blue circles are the corresponding estimates of the debiased TV estimator. 4a Ground truth image with rectangle for showing confidence intervals for pixels in the rectangle 4b Reconstruction with 7% noise and 50% radial subsampling 4c Reconstruction with 11% noise and 50% radial subsampling 4d Reconstruction with 7% noise and 50% spiral subsampling 4e Reconstruction with 11% noise and 50% spiral subsampling.

containing prostate images; information on this dataset is provided in a short arXiv version [10] and in an extended journal version here [11]. In contrast to the image we used in the main part of the paper, here, the ground truth images are real-valued. We used ground truth images from the single-coil knee dataset; for the brain and prostate datasets, we used T2-weighted images from the multi-coil dataset. First, we cropped all images to the size 320×320 and then applied a Fourier transform and a radial or spiral mask. The experiments were conducted for every body part for 30 images from 6 patients. We conducted experiments for the radial mask with undersampling 50% and 70% and for the spiral mask with undersampling 33% and 50%. The hit rates of the confidence intervals $99\%, 95\%, 92.5\%$ for those body parts are calculated and presented in boxplots in Fig. 2. One can see that the hit rates are slightly higher for the prostate and the brain than for the knee dataset for every confidence level and acceleration factor. This is due to the different sparsity levels of the gradient for different MR modalities. This implies that the boxes for the knee dataset, representing the variance of the hit rates, are larger. Moreover, a few dots, representing outliers, are visible outside the box plots. This is probably due to more diverse MRI slices for the knee. Other than that, one can see that all hit rates are higher than the desired confidence levels, which confirms that the prediction is good. We did not conduct the experiments for different noise levels; if one uses less noise, the

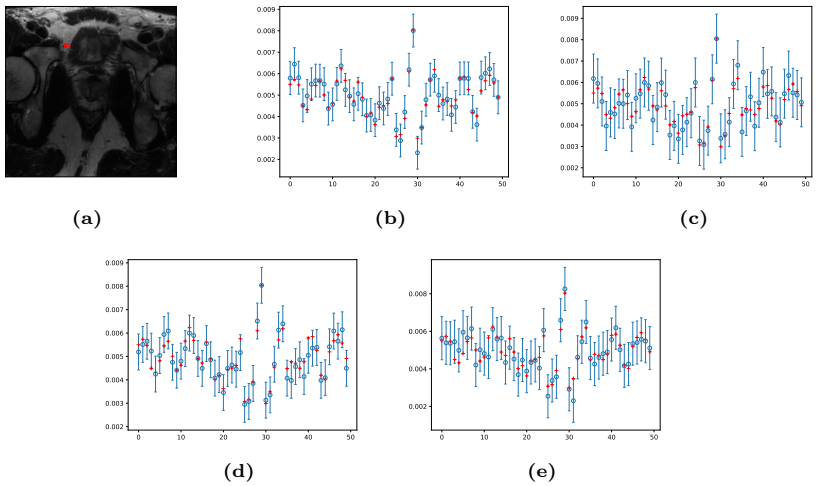

Fig. 5: Confidence intervals for a prostate image from the fastMRI multi-coil dataset [10, 11] for spiral and radial masks and different noise realizations. 95% confidence intervals for the magnitude of pixels in the rectangle. The red crosses are the ground truth values, and the blue circles are the corresponding estimates of the debiased TV estimator. 5a Ground truth image with rectangle for showing confidence intervals for pixels in the rectangle 5b Reconstruction with 7% noise and 50% radial subsampling 5c Reconstruction with 11% noise and 50% radial subsampling 5d Reconstruction with 7% noise and 50% spiral subsampling 5e Reconstruction with 11% noise and 50% spiral subsampling.

hit rates worsen since the noise level and the reconstruction accuracy are not linearly related. On the other hand, if we add more noise, the hit rates will get better.

As in the main paper for the complex brain image, we show here the confidence intervals for one knee, brain, and prostate image for a small region taken from these images; see Figures 3, 4 and 5. These figures show confidence intervals for both the spiral and radial mask with 50% undersampling and 7% and 11% noise. It is well visible that the confidence intervals get larger when we increase the noise and as the reconstruction error does not increase linearly with the noise level, the hit rates for 11% noise are better than the ones for 7% noise. Therefore, more ground truth pixels lie in the confidence interval. Furthermore, one can observe in the figures that the spiral mask works slightly better than the radial mask, but both generally work well. For higher undersampling rates, the reconstruction is better; therefore, the hit rates are higher (more red crosses on the blue lines); for lower undersampling rates, the reconstruction is worse, which would also cause the hit rates to get lower. The above experiments show that our method works for several body parts, acceleration factors, patients, and confidence levels.

Table 1: Spiral sampling of real-world MRI data: Results are averaged over $l = 100$ realizations of the noise. The underlying image is normalized, i.e., $\|x^0\|_2 = 1$. Split-Bregman was performed with 1000 outer and 50 inner iterations.

m	$0.43N$		$0.62N$	
rel noise	0.10	0.065	0.12	0.08
$\mathrm{SSIM}(\hat{x}, x^0)$	0.8242	0.887	0.8607	0.9188
$\|\hat{x} - x^0\|_\infty$	0.0052	0.0043	0.0042	0.0033
$\|\hat{x} - x^0\|_2$	0.1203	0.1035	0.1021	0.0836
$\|\hat{x}^u - x^0\|_\infty$	0.0052	0.0039	0.0042	0.0029
$\|\hat{x}^u - x^0\|_2$	0.2411	0.1704	0.1936	0.1335
$\|R\|_\infty$	0.0033	0.0029	0.0018	0.0017
$\|R\|_2$	0.1362	0.1171	0.0810	0.0700
$\|W\|_\infty$	0.0052	0.0034	0.0041	0.0027
$\|W\|_2$	0.2480	0.1655	0.1954	0.1302
$h(0.05)_S$	0.9453	0.9064	0.9455	0.9251
$h(0.05)$	0.9573	0.9382	0.9525	0.9418

References

1. Aja-Fernández, S., Vegas-Sánchez-Ferrero, G.: Statistical Analysis of Noise in MRI: Modeling, Filtering and Estimation. Springer, Cham (2016). https://doi.org/10.1007/978-3-319-39934-8
2. Beck, A., Teboulle, M.: A fast iterative shrinkage-thresholding algorithm for linear inverse problems. SIAM journal on imaging sciences **2**(1), 183–202 (2009). https://doi.org/10.1137/080716542
3. Briggs, W.L., Henson, V.E.: The DFT: an owner's manual for the discrete Fourier transform. SIAM (1995). https://doi.org/10.1137/1.9781611971514
4. Chambolle, A., Caselles, V., Cremers, D., Novaga, M., Pock, T., et al.: An introduction to total variation for image analysis. Theoretical foundations and numerical methods for sparse recovery **9**(263-340), 227 (2010). https://doi.org/10.1515/9783110226157.263
5. Genzel, M., Macdonald, J., März, M.: Solving Inverse Problems With Deep Neural Networks – Robustness Included? IEEE Transactions on Pattern Analysis and Machine Intelligence **45**(1), 1119–1134 (2023). https://doi.org/10.1109/TPAMI.2022.3148324
6. Goldstein, T., Osher, S.: The split Bregman method for L1-regularized problems. SIAM journal on imaging sciences **2**(2), 323–343 (2009). https://doi.org/10.1137/080725891
7. Knoll, F., Zbontar, J., Sriram, A., Muckley, M.J., Bruno, M., Defazio, A., Parente, M., Geras, K.J., Katsnelson, J., Chandarana, H., Zhang, Z., Drozdzalv, M., Romero, A., Rabbat, M., Vincent, P., Pinkerton, J., Wang, D., Yakubova, N., Owens, E., Zitnick, C.L., Recht, M.P., Sodickson, D.K., Lui, Y.W.: fastMRI: A Publicly Available Raw k-Space and DICOM Dataset of Knee Images for Accelerated MR Image Reconstruction Using Machine Learning. Radiology: Artificial Intelligence **2**(1), e190007 (2020). https://doi.org/10.1148/ryai.2020190007, https://doi.org/10.1148/ryai.2020190007, pMID: 32076662

Table 2: Real-world sampling with radial mask: Results are averaged over $l = 100$ realizations of the noise. The underlying image is normalized, i.e., $\|x^0\|_2 = 1$. Split-Bregman was performed with 500 outer and 50 inner iterations.

m	$0.5N$		$0.7N$		$0.9N$	
rel noise	0.105	0.07	0.125	0.08	0.14	0.095
$\mathrm{SSIM}(\hat{x}, x^0)$	0.8319	0.8938	0.8572	0.9152	0.8793	0.930
$\|\hat{x} - x^0\|_\infty$	0.0047	0.0037	0.0039	0.0029	0.00034	0.0024
$\|\hat{x} - x^0\|_2$	0.1100	0.0926	0.0975	0.0782	0.0902	0.0698
$\|\hat{x}^u - x^0\|_\infty$	0.0047	0.0034	0.0038	0.0027	0.0033	0.0022
$\|\hat{x}^u - x^0\|_2$	0.2182	0.1524	0.1813	0.1237	0.1576	0.1056
$\|R\|_\infty$	0.0024	0.0022	0.0013	0.0012	0.0006	0.0005
$\|R\|_2$	0.1106	0.0955	0.0649	0.0557	0.0274	0.0235
$\|W\|_\infty$	0.0047	0.0031	0.0038	0.0025	0.0033	0.0022
$\|W\|_2$	0.2239	0.1492	0.1830	0.1220	0.1584	0.1056
$h(0.05)_S$	0.9468	0.9195	0.9482	0.9362	0.9504	0.9477
$h(0.05)$	0.9565	0.9420	0.9527	0.9455	0.9514	0.9498

8. Paige, C.C., Saunders, M.A.: Lsqr: An algorithm for sparse linear equations and sparse least squares. ACM Transactions on Mathematical Software (TOMS) **8**(1), 43–71 (1982)
9. Ravasi, M., Vasconcelos, I.: PyLops—A linear-operator Python library for scalable algebra and optimization. SoftwareX **11**, 100361 (2020). `https://doi.org/https://doi.org/10.1016/j.softx.2019.100361`
10. Tibrewala, R., Dutt, T., Tong, A., Ginocchio, L., Keerthivasan, M.B., Baete, S.H., Chopra, S., Lui, Y.W., Sodickson, D.K., Chandarana, H., et al.: Fastmri prostate: A publicly available, biparametric mri dataset to advance machine learning for prostate cancer imaging. arXiv preprint arXiv:2304.09254 (2023)
11. Tibrewala, R., Dutt, T., Tong, A., Ginocchio, L., Lattanzi, R., Keerthivasan, M.B., Baete, S.H., Chopra, S., Lui, Y.W., Sodickson, D.K., et al.: Fastmri prostate: A public, biparametric mri dataset to advance machine learning for prostate cancer imaging. Scientific Data **11**(1), 404 (2024)
12. Zbontar, J., Knoll, F., Sriram, A., Murrell, T., Huang, Z., Muckley, M.J., Defazio, A., Stern, R., Johnson, P., Bruno, M., Parente, M., Geras, K.J., Katsnelson, J., Chandarana, H., Zhang, Z., Drozdzal, M., Romero, A., Rabbat, M., Vincent, P., Yakubova, N., Pinkerton, J., Wang, D., Owens, E., Zitnick, C.L., Recht, M.P., Sodickson, D.K., Lui, Y.W.: fastMRI: An Open Dataset and Benchmarks for Accelerated MRI (2019)